Title

Spatiotemporal Patterns of Precipitation-Modulated Landslide Deformation From Independent Component Analysis of InSAR Time Series

Journal

Geophysical Research Letters, 45(4)

ISSN

0094-8276

Authors

Cohen-Waeber, J
Bürgmann, R
Chaussard, E
et al.

Publication Date

2018-02-28

DOI

10.1002/2017gl075950

Peer reviewed

Spatiotemporal Patterns of Precipitation-Modulated Landslide Deformation From Independent Component Analysis of InSAR Time Series

J. Cohen-Waeber[1] , R. Bürgmann[2] , E. Chaussard[3] , C. Giannico[4] , and A. Ferretti[4]

[1] Department of Civil and Environmental Engineering, University of California, Berkeley, CA, USA, [2] Berkeley Seismology Laboratory and Department of Earth and Planetary Science, University of California, Berkeley, CA, USA, [3] Department of Geology, State University of New York at Buffalo, Buffalo, NY, USA, [4] TRE ALTAMIRA, Milan, Italy

Correspondence to: J. Cohen-Waeber, jwaeber@berkeley.edu

Abstract

Long-term landslide deformation is disruptive and costly in urbanized environments. We rely on TerraSAR-X satellite images (2009–2014) and an improved data processing algorithm (SqueeSAR™) to produce an exceptionally dense Interferometric Synthetic Aperture Radar ground deformation time series for the San Francisco East Bay Hills. Independent and principal component analyses of the time series reveal four distinct spatial and temporal surface deformation patterns in the area around Blakemont landslide, which we relate to different geomechanical processes. Two components of time-dependent landslide deformation isolate continuous motion and motion driven by precipitation-modulated pore pressure changes controlled by annual seasonal cycles and multiyear drought conditions. Two components capturing more widespread seasonal deformation separate precipitation-modulated soil swelling from annual cycles that may be related to groundwater level changes and thermal expansion of buildings. High-resolution characterization of landslide response to precipitation is a first step toward improved hazard forecasting.

Plain Language Summary

In an ever-expanding urban environment, we opt to live with the risk of catastrophic natural hazards through a perceived safety net of building codes and engineering solutions. Unfortunately, our concern for these hazards is often focused on their immediate impact to our everyday lives and does not account for imperceptible processes that may become significant over decades in time. Notoriously, some landslides slowly and continuously deform, ultimately causing costly unpredicted damage to homes, lifelines, and other infrastructure. Recent advances in satellite technology allow us to accurately measure these long-term movements, tracking where and when they occur. We show that the duration and amount of seasonal precipitation and associated water pressure changes determine how fast the landslides move and how recent drought conditions have slowed their advance. The satellite data allow us to differentiate the landslide deformation from normal

seasonal changes in unaffected areas, giving us greater predictability of this hazard.

1 Introduction

Interferometric Synthetic Aperture Radar (InSAR) time series analysis allows for remote detection and characterization of ground surface displacements with subcentimeter precision and accuracy and tens of meters of spatial resolution (Bürgmann et al., 2000), making it particularly suitable for the study of active slow-moving landslides (Colesanti & Wasowski, 2006; Tofani et al., 2013; Wasowski & Bovenga, 2014). Its application has been shown to successfully track seasonally modulated landslide deformation (Handwerger et al., 2013). In the San Francisco East Bay Hills (EBH), previous analyses of InSAR data sets from different satellites over several periods between 1992 and 2006 (Hilley et al., 2004; Quigley et al., 2010) focused on defining the spatial extent of known active landslides, resolving consistent average downslope displacement rates (~25–39 mm/year), and revealing the average time lag between maximum winter precipitation and peak landslide velocity (~1–3 months).

It is well understood that pore pressure is the primary driving factor of landslides (Terzaghi, 1950) and seasonal slide rate changes are tied to precipitation-driven transient pore pressure increases (Iverson & Major, 1987). Without sufficient characterization of subsurface conditions to quantify pore pressure changes, we rely on a simple 1-D diffusion model to infer pore pressure changes from precipitation and characterize their seasonal and long-term effects on ground motion. We produce InSAR time series with substantially improved temporal resolution and an enhanced analysis algorithm (SqueeSAR™) to capture the full spatiotemporal response patterns of ground deformation to annual precipitation cycles and multiyear drought conditions for the Blakemont landslide (BLS) in the northern EBH. In doing so, we expose the underlying dynamics of the observed deformation by adopting a statistical signal processing approach to isolate the processes which add up to the observed deformation without a priori constraints.

The EBH are a northwest trending, uplifted block of Jurassic to Tertiary sedimentary, volcanic, and metamorphic rocks, folded in a synclinal form during regional transpression, beginning 1–2 million years ago (Graymer, 2000) and are now largely overlain by Quaternary colluvial and alluvial deposits. The BLS has been well described (Bishop et al., 1973; Dibblee, 1980; Graymer et al., 1994; Kropp & Lettis, 2002; Seidelman & Deane, 1994) as a very slow-moving, earthflow-type landslide complex (Cruden & Varnes, 1996) of approximately 0.88 km^2. It is composed of highly expansive clays and sandy clays to depths of approximately 3 m, underlain by gravels, clays, and clays with rock fragments. Deeper landslide debris (8 to ~22 m) are composed of mixtures of hard blocks from the Franciscan Complex bedrock within a weaker sheared matrix of clay and shale. Independent estimates of landslide depth and subsurface investigations (Text S1 and Figure S1 in the

supporting information) concur that active deformation is distributed within the upper ~10 m of the slide mass with displacement occurring along distinct shear zones (Kropp & Lettis, 2002). The active slide mass exhibits typical hummocky topography and springs in predevelopment air photos from the 1930s (Figure S2). The BLS now affects nearly 135 property parcels, causing structural damage to homes and regularly disrupting underground utilities.

Landslide mobility in the EBH is primarily driven by a wet microclimate from local orographic precipitation (Beaty, 1956; Gilliam, 2002). Precipitation rates are strongly seasonal, with little rainfall between May and October (Nilsen & Turner, 1975). The precipitation data for this study were gathered at the Lawrence Berkeley National Laboratory, at the southeast end of our study area. The average seasonal precipitation since 1974 is 76.5 cm but was above average during the winter months of 2010 and 2011 with 84 and 94 cm, respectively. During the period of 2012–2014, California experienced extreme drought conditions (Seager et al., 2015), reflected in cumulative precipitation of only 48 cm during the winter season of 2013/2014.

Seismic shaking from nearby faults may also be expected to trigger accelerated landslide displacements (Keefer & Johnson, 1983; Lacroix et al., 2014), although a clear relationship between seismicity and landslide activity has yet to be established in the EBH. The right-lateral strike-slip Hayward fault (HF) traverses the head of each major landslide in our study area, and has the potential for an Mw 7.0 event (Chaussard et al., 2015; Field & 2014-WGCEP, 2015). While Hilley et al. (2004) suggest that an HF Mw 3.9 event in December 1998 induced downslope displacements, no evidence of seismically induced landslide displacements could be determined in our time series analysis from an Mw 4.0 event in March 2012, located only 2 km northwest of the first. Furthermore, no evidence of accelerated displacements was documented due to any of the large historic earthquakes in the region, since 1868 (Figure S1).

Here we investigate the controls of observed time-dependent deformation at the BLS through an independent component analysis (ICA) of InSAR time series. We use 119 German Aerospace Center (DLR) TerraSAR-X (TSX) satellite scenes (Eineder et al., 2009) collected along descending track 38 from 2009 to 2014, with repeat pass cycles as short as 11 days (Text S2, Figure S3, and Table S1 in the supporting information). Using functional curve fitting (FCF) and principal component analyses (PCAs), we establish that four modes of temporal and spatial variabilities exist in the observed surface ground motions, which are tied to annual and multiyear precipitation cycles. ICA allows us to optimally separate these four spatiotemporal patterns and their contributions to the original signal. We illustrate the utility of these methods by relating the observed patterns of ground motion to the underlying driving mechanisms of slope displacement, specifically isolating precipitation-correlated landslide deformation that is directly linked to time dependent pore pressure changes.

2 Methods

2.1 InSAR Processing

The high spatial resolution of InSAR, particularly that of X-band imagery in urbanized environments, makes it a valuable tool for monitoring the details of mm-scale surface deformation of slow moving (<20 mm/yr) landslides (Wasowski & Bovenga, 2014). InSAR time series represent a record of change in radar signal return phase over time, mostly reflecting the change in line-of-sight (LOS) distance (range) between the ground surface and the radar platform. Persistent or permanent scatterer InSAR time series analysis techniques are based on finding pixels whose amplitude and/or phase properties are stable through time (Ferretti et al., 2001; Hooper et al., 2012). The algorithm SqueeSAR™ (Ferretti et al., 2011) relies on a statistical test (two-sample Kolmogorov-Smirnov) to partition image pixels into PSs with stable amplitude properties and coherent signal phase and additional phase-stable distributed scatterers. Here the PSs are processed in the manner described in Ferretti et al. (2001), and the distributed scatterers are integrated in the same processing chain taking into account their different statistical behavior (Ferretti et al., 2011), thus increasing the measurement point (MP) density (6,228.1 MP/km^2) by roughly 1 order-of-magnitude (Figure S4) from that shown in Hilley et al. (2004).

For each MP, a deformation time series is produced from the 119-scene data stack, using 118 interferograms with respect to a central reference image (Figure S3) and a stable reference point, located southwest of the BLS on the roof of a large three-story building (lat: 37.90747°, lon: −122.29453°). While the reference point was selected in an area that is consistently stable with low-amplitude signal throughout the time series, the measured signal in all MPs inherently includes its background temporal variability. Atmospheric and other noise sources were mitigated as described in Ferretti et al. (2001).

2.2 Analysis of Time-Dependent and Precipitation-Modulated Deformation

In order to reveal the different seasonal and long-term transient spatiotemporal patterns within our data, we use a combination of signal processing analysis methods that are detailed in Text S3. For a first-order estimate of the temporal periodicity and amplitude of the observed time series, we apply the linear sum of several a priori functions to fit the MP time series (FCF) within and around the BLS. To separate the spatial patterns of dominant long-term, seasonal, and other common-mode variations in the surface deformation field without assuming functional forms of their time dependence, we apply both PCA and ICA.

Temporal-mode PCA (Richman, 1986) finds the linear transformations, or principal components (PCs), that best fit the maximum variance in a set of variables. The result is a set of uncorrelated PCs ordered by the percentage of variance explained and limited by an orthogonal basis which captures the variance most efficiently but may also miss and mix some part of the data

trends. In contrast, ICA maximizes the statistical independence of an arbitrary number of independent components (ICs), to fit different spatial patterns and temporal functions (Gualandi et al., 2017). The result is a set of optimized ICs that describe the underlying data trends, but the ideal number of ICs and their order of importance are not defined. Therefore, we utilize both methods in a complimentary fashion, to determine the number and rank of necessary components (by PCA) and to optimally describe the data's spatiotemporal patterns (by ICA).

Results of the component analyses are presented as eigenvalue (or coefficient) time histories for each PC or IC, corresponding to the variance or the independence of that component and the magnitude of its contribution at each time step. These are plotted alongside a corresponding score map of all MPs, illustrating the spatial variability of each component and corresponding to its contribution to the original data at that point. The product of the score value of each MP by the scaled eigenvalue at any given time gives the contribution of that component in deformation units at that time.

3 Results

3.1 Velocity Field and Background Signals From InSAR Analysis

Figure 1 illustrates the average MP LOS velocities across the EBH with respect to the reference point. The data reveal the active portions of historically mapped landslides, ~5 mm/yr of shallow aseismic slip along the NW-trending HF (Chaussard et al., 2015; Shirzaei & Bürgmann, 2013) and settlement of man-made landfill along the San Francisco Bay coastline to the west. Using the LOS velocity field, we determine the spatial extent of active EBH landslides by clusters of MPs (>10) with velocities exceeding the mean velocity of the study area by one standard deviation (<−2 mm/yr LOS). While the resulting active slide areas generally match previously mapped slide masses (Hilley et al., 2004; Kropp, 1995; Quigley et al., 2010), we find that the improved MP density resolves the landslide boundaries and displacement fields in much greater detail (Figure S1).

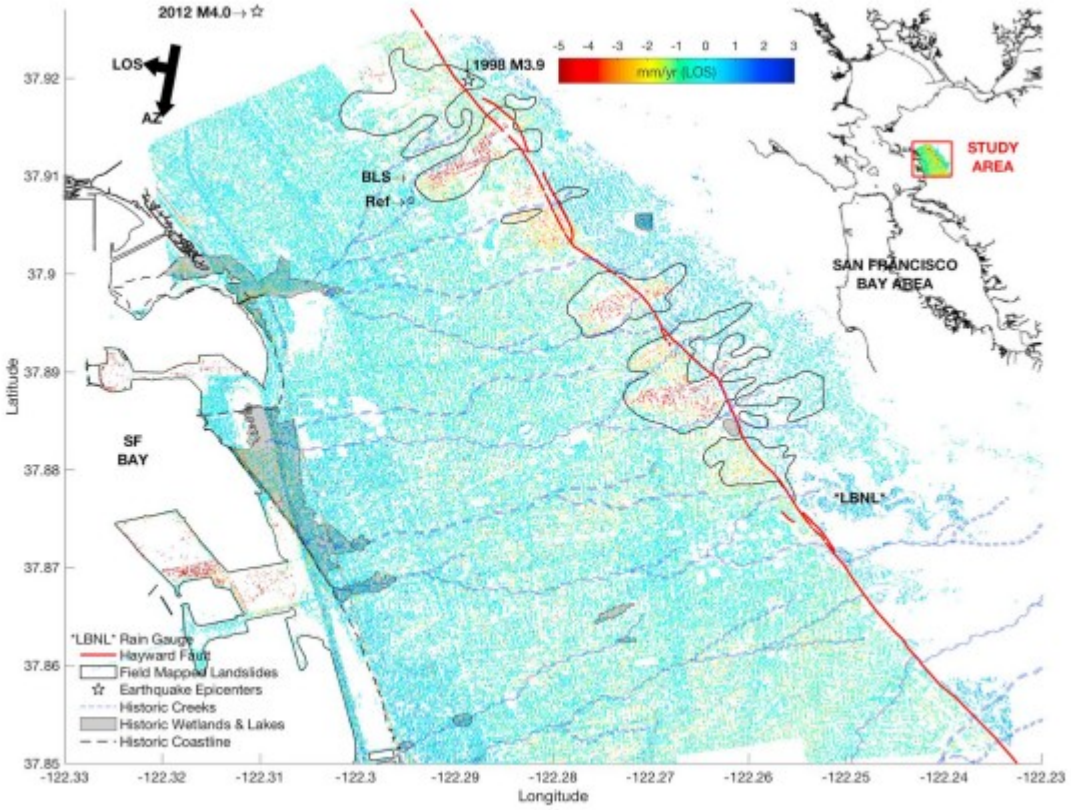

Figure 1

TerraSAR-X mean line-of sight range-change velocity map of the East Bay Hills area obtained from the SqueeSAR™ analysis, showing motion relative to the reference point (Ref). The positive values (blue colors) show motion toward the satellite (i.e., uplift or eastward movement), and the negative values (red colors) show motion away from the satellite (i.e., subsidence or westward movement).

Without at least three independent LOS observations, it is not possible to resolve the three-dimensional sense of landslide motion (Delbridge et al., 2016). However, an estimate of the magnitude of actual ground displacement can be made by assuming a downslope orientation of landslide motion. Downslope velocities ranging between 27 and 39 mm/yr are obtained (Text S2 and Figure S5), roughly −3.9 times the LOS displacement and similar to previous studies. While there are few quantitative measurements of motion prior to the 1990s, it appears that the landslides have moved at comparable rates for many decades (Kropp, 2010; Kropp & Lettis, 2002).

3.2 Time-Dependent Surface Displacements From FCF, PCA, and ICA

Figure 2 summarizes the results of the ICA, using four components (IC1–IC4), which optimally isolate the major spatial and temporal trends underlying the deformation time series. We initially identify these controlling modes of variability on and off the active BLS (mapped in Figure 2a, right) through a combination of FCF and PCA. FCF highlights three first-order trends showing seasonally precipitation-modulated accelerations of landslide displacement

with a 30–40 day lag (Figure 2a, left, red triangles and black squares), a multiyear deceleration in the same landslide deformation caused by the onset of regional drought conditions in 2012, and a notably cyclic background seasonal signal in all MP time histories revealed by the average off-landslide motion (Figure 2a, left, blue triangles). Using temporal-mode PCA, we are able to determine that these first-order trends are best captured by four uncorrelated PCs that account for ~91% of the signal variance. Ultimately, we apply ICA to optimize these four spatiotemporal patterns into statistically independent ICs which we describe here. A detailed description of the FCF and PCA results is included in Texts S4 and S5, respectively.

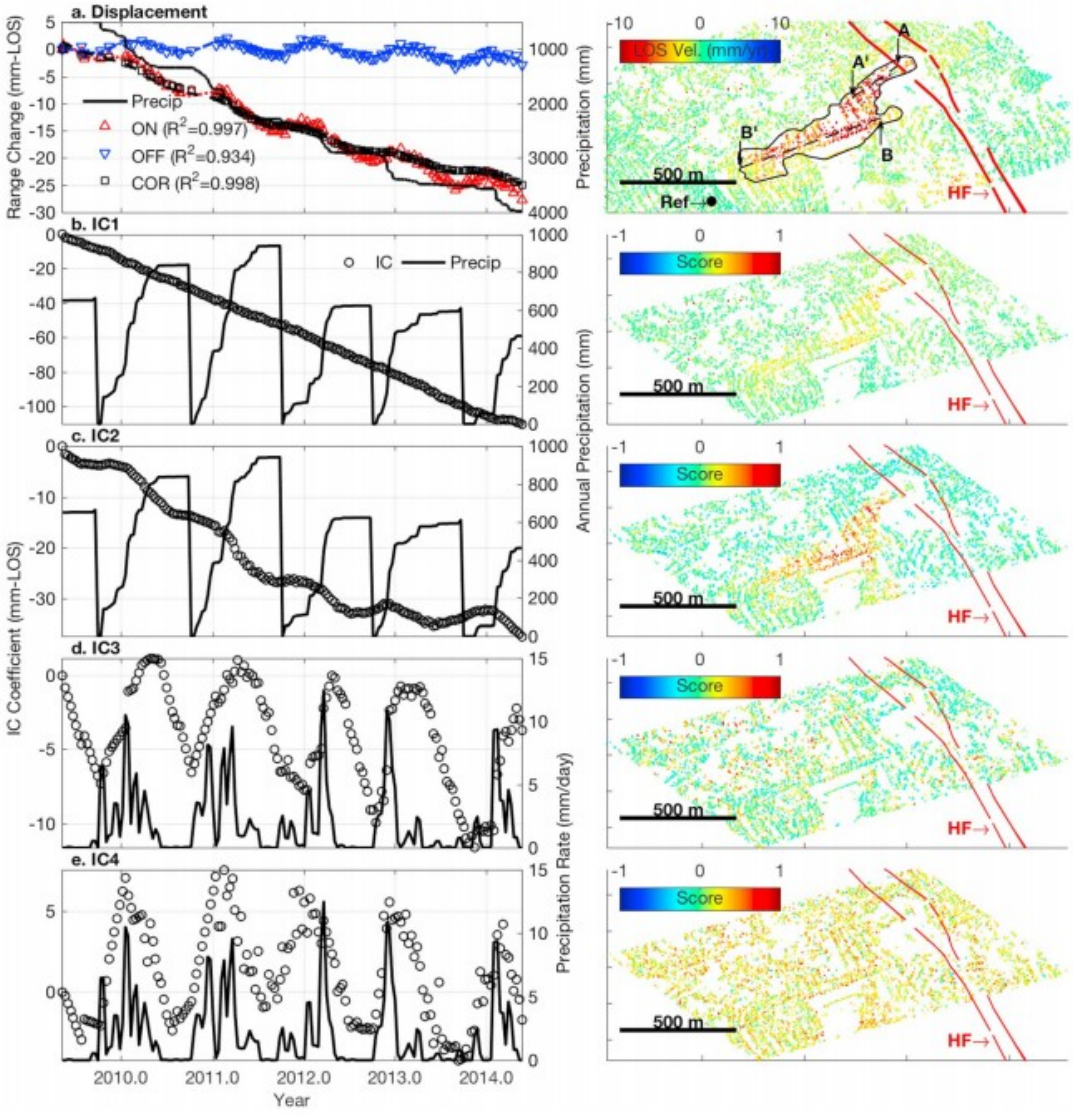

Figure 2

(a) (left) Functional curve fitting results for the Blakemont landslide (BLS) of average “ON landslide” (red triangles), “OFF landslide” (blue triangles), and “CORrected (ON-OFF) landslide” (black squares) displacement time histories. (right) line-of sight velocity map of the BLS area with the “active” BLS deposit defined by measurement point velocities <−2 mm/yr. (b–e) independent component analysis

results for the BLS showing eigenvalue time series for each independent component scaled by the percent nonzero eigenvalues retained (left, circles) and their corresponding score maps (right). Precipitation (solid black lines) is shown in the left panels as total cumulative (a), water-year cumulative (October–September) (b and c), or daily rates (d and e).

Figures 2b–2e describe the ICA results for the BLS, showing eigenvalue time series for each IC (left, circles) plotted against precipitation (left, solid lines) and their corresponding score maps (right). For clarity and comparison, each score map has been normalized by its relative maximum and factored into the eigenvector (IC) time series. The time series have also been corrected for the percentage of data explained (~95.7%). As such, the product of the MP score values and their corresponding eigenvalues (ICs) in Figure 2 will return the contribution of each component in deformation units (mm). Using less or more components, we find that parts of the different signals are either superimposed or result in less distinct time series and featureless score maps in the extra components.

Independent components 1 and 2 (Figures 2b and 2c, respectively) show positive scores on the BLS, indicating downward and westward displacements (negative eigenvector slope), with negligible contribution from points outside the BLS footprint. IC1 describes a nearly linear deformation time history with no seasonal variability, while IC2 describes seasonal accelerations directly correlated to peak seasonal precipitation rates, and a reduction in displacement rate with the onset of the drought in 2012. The combination of these two components and their score maps returns the same average displacement time series describing precipitation-modulated landslide motion as the “corrected” (black squares) curve from the FCF analysis (Figure 2a). To better illustrate both spatial and temporal seasonal variations in the BLS velocity field, we plot the velocity time history along a 100 m wide swath (Figure 2a, right) against the rate of precipitation (Figure 3). Spatial variations in the velocity field clearly show which portions of the slide remain active throughout (e.g., ~320 m), while others slow or stop. Figure 3 also captures the response time of displacement to precipitation for different parts of the landslide (30–40 day lag) and the significance of drought effects since 2012, with shorter periods of landslide activity sometimes slowing to a halt (e.g., 500 to 600 m).

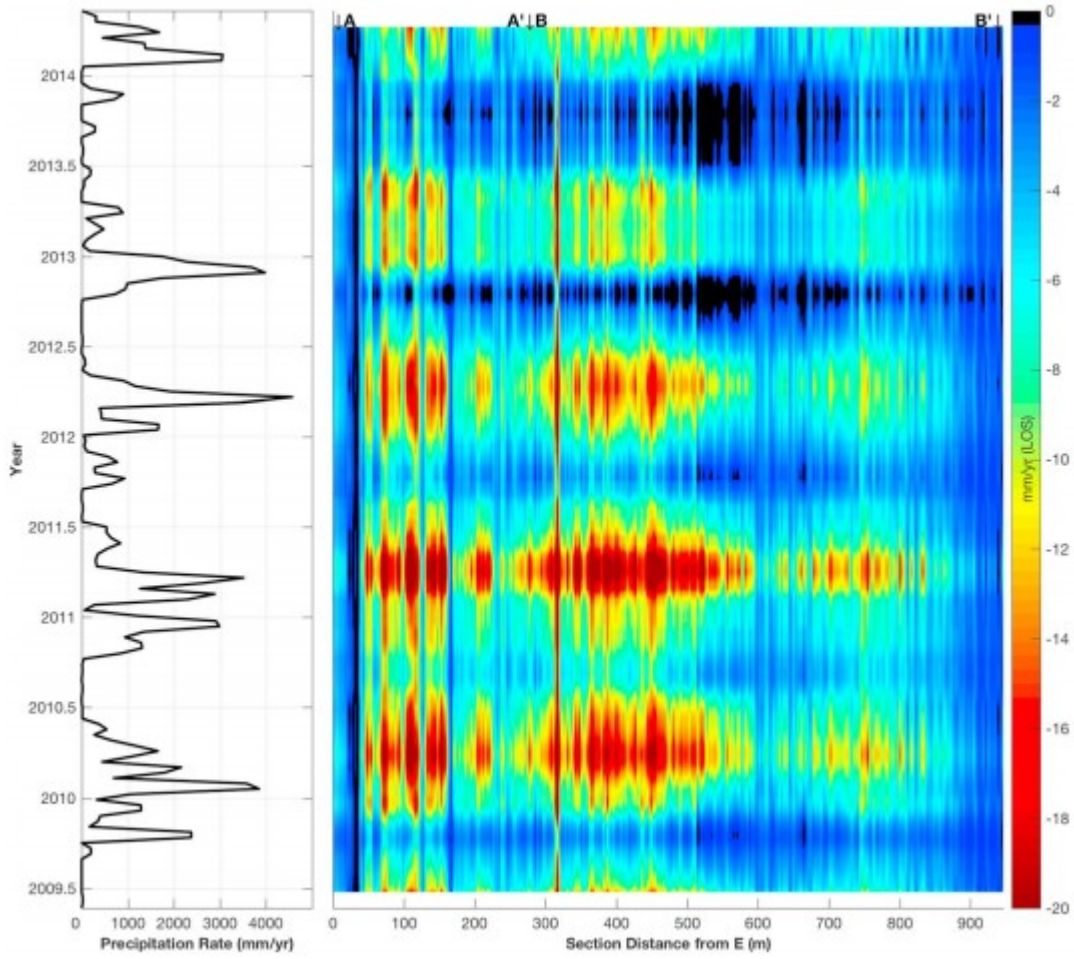

Figure 3

Time series of spatial variability in the velocity field along a 100 m wide swath from top to bottom (Figure 2a, right) of the Blakemont landslide (BLS), reconstructed from independent components 1 and 2. Animation S1 shows the velocity time history for all measurement points on the BLS.

The IC3 and IC4 score maps describe a broadly distributed signal, both on and off the BLS (Figures 2d and 2e, respectively). The eigenvector time series describe seasonal deformation with precipitation-modulated ground displacements, where positive slopes (in combination with the positive score values) describe uplift/eastward motion (toward the satellite). While the eigenvector time series in IC3 shows a positive correlation to seasonal precipitation that is highly sensitive to the peak periods of precipitation, IC4 shows a positive correlation to the rate of precipitation with a phase lag from IC3 of approximately 3–4 months.

It becomes evident that while the processes in IC3 and IC4 are best described by the phase and amplitude of their seasonal deformation with precipitation rates, IC1 and IC2 are landslide processes controlled by transient pore pressures acting within the slide body and best described by their rates of change. Assuming that the rate of precipitation controls the

surface boundary condition for pore pressure, we define a one-dimensional solution for the diffusion equation (Handwerger et al., 2016) as a function of depth and time (Text S6). Based on the velocity time series and a maximum depth of sliding (~15 m), we estimate a first-order value of diffusivity (~1.5 $\times 10^{-6}$) and calculate a transient pore pressure time history at established active depths of sliding ~6 m (Figures S10–S11).

A cross-correlation analysis of the IC eigenvector time series with precipitation rates and transient pore pressures quantifies the observed seasonal effects on surface deformation (Figure 4). Combining IC1 and IC2, we reconstruct a landslide deformation time series and compare the rate of surface deformation with transient pore pressure at ~6 m (Figure 4a) and the rate of precipitation (Figure 4b). The cross-correlation between the rate of IC1 + IC2 and modeled pore pressure is positive with zero lag. The cross-correlation between the rate of IC1 + IC2 and the rate of precipitation illustrates the delayed seasonal response of landslide displacement, with a positive lag of 44 days. Due to its sensitivity to peak precipitation events, the correlation between the rate of IC3 deformation and the rate of precipitation (zero lag) masks its underlying behavior. Cross-correlating the IC3 eigenvector time series with precipitation (Figure 4c) reveals that it is also strongly correlated to seasonal onsets with upward movement occurring as long as precipitation persists, followed by a drawn-out recovery through the dry season. The 66–77 day lag coincides well with the onset of the dry season approximately 2–3 months after peak seasonal precipitation. IC4, on the other hand, reveals a positive correlation to precipitation with only an 11 day lag, suggesting that it is more directly tied to the timing and amount of precipitation (Figure 4d).

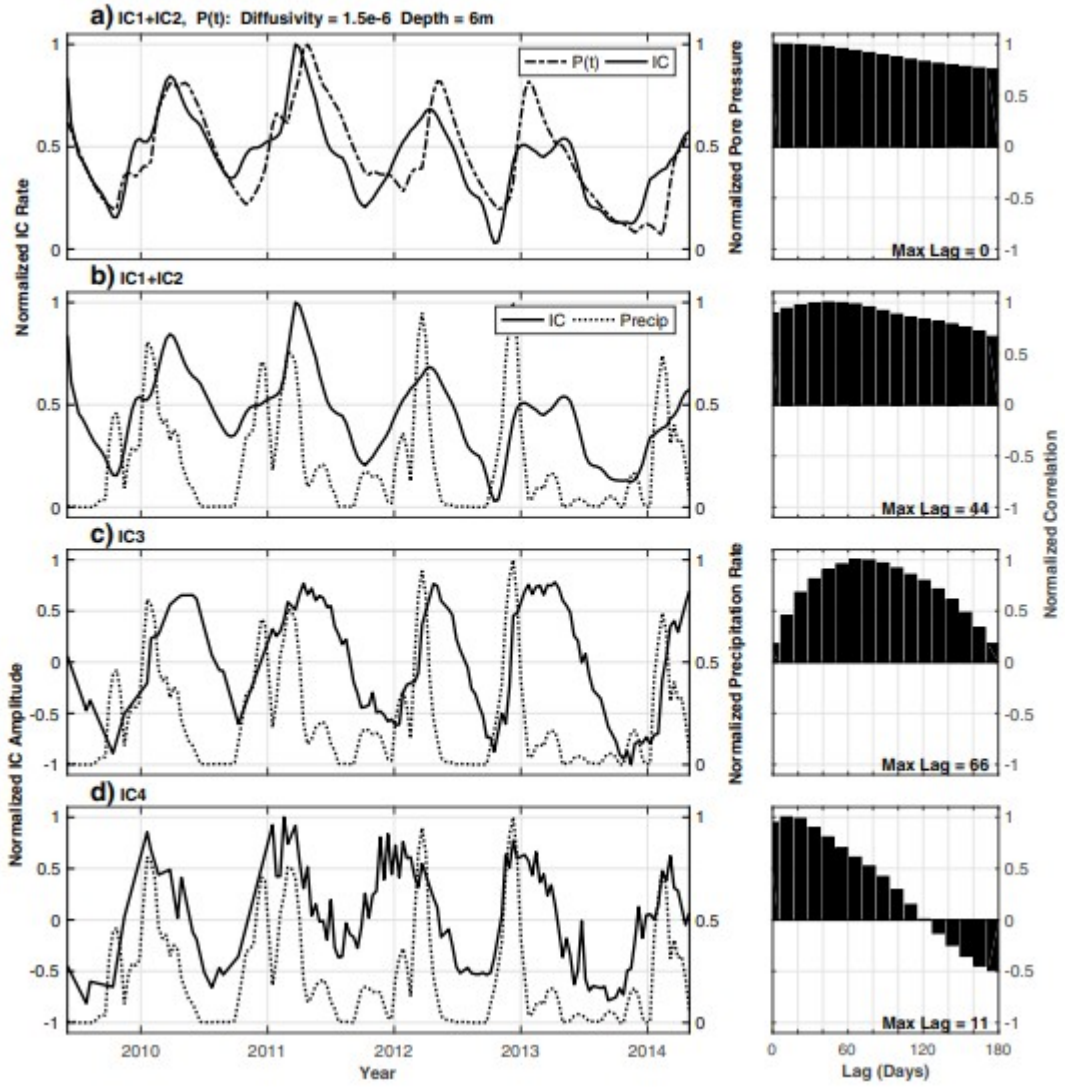

Figure 4

Results of the cross-correlation (right, bars) between the independent component (IC) eigenvector time series (left, solid), transient pore pressures $P(t)$ (left, dashed), and precipitation rates (left, dotted). The rate of IC1 + IC2 describing changes in landslide velocity is (a) positively correlated to transient pore pressures with zero lag and (b) positively correlated to precipitation with a 44 day time lag. Deformation described by (c) IC3 is positively correlated to seasonal precipitation with a 66–77 day lag, and (d) IC4 is positively correlated to precipitation with an 11 day lag.

4 Discussion

The dense SqueeSAR™ MP coverage in our study area accurately documents several surface deformation features in the EBH including the spatial extent of active landslides (Figures 1and S1). Our goal is to separate the spatial and temporal patterns of dominant long-term, seasonal, and other common-mode variations of displacement and to isolate the responsible processes. The ICA does this by maximizing the independence of components such that they must represent different spatiotemporal patterns. We find that seasonal

precipitation is the primary factor in modulating deformation on and off the BLS. The spatial distribution of motions across the landslide body vary (Figure 3 and Animation S1 in the supporting information), illustrating the heterogeneous nature of the slide mass, supporting its characterization as an earthflow type slide complex and capturing its spatially variable response to precipitation-modulated transient pore pressures in IC1 and IC2.

The broadly variable spatial distribution of IC3 and IC4 (Figures 2d and 2e) suggests that their seasonal signal is tied to general soil and hydrological deformation processes. We propose that IC3 is primarily tied to shrink-swell cycles of surficial soils that are sensitive to both the amount and occurrence of precipitation (Ng et al., 2003; Rosenbalm, 2013). A reversal in surface deformation is tied to the end of each wet season, when evapotranspiration begins to drive progressive shrinking. In contrast, the eigenvector time history in IC4 illustrates ground surface deformation directly correlated to the rate of precipitation with a short lag time and little variability during dry months (Figure 4d). While we have no concurrent groundwater level data for the observation period, groundwater levels in the EBH can fluctuate by several meters (Kropp & Lettis, 2002; Seidelman & Deane, 1994) and we interpret this component as the poroelastic response to shallow precipitation-driven groundwater-level changes (Chaussard et al., 2014). Alternatively, IC4 is also strongly anticorrelated with seasonal temperature variations. Thermal expansion of buildings, including the reference point, during warm summer months may contribute to this component but is likely to be small.

The TSX deformation time series reveal the direct response of landslide motion to short-term, seasonal, and multiyear changes in precipitation. While their processes are mechanically related, IC1 and IC2 (Figures 2b and 2c) isolate the sensitivity of landslide-related ground displacements to these climate-driven cycles. We observe three distinct temporal trends. First, IC1 (Figure 2b) reflects continuous creep deformation unaffected by seasonal variations at an average LOS rate of −3.5 mm/yr. Next, IC2 (Figure 2c) demonstrates both longer-term and seasonal landslide velocity changes. A distinct reduction in the average IC2 velocity occurs in 2012, quantifying the effects of drought conditions on slide displacement (Bennett et al., 2016). As EBH seasonal precipitation decreases from ~90 to ~60 cm, average LOS rates slow by ~2 mm/yr (~75%). IC2 also quantifies the sensitivity of the BLS to seasonal precipitation, where precipitation enhanced LOS rates reach −8 mm/yr during peak wet seasons and slow or stop during peak dry seasons. Combined, IC1 and IC2 closely match the corrected “on-slide” time series (Figure 2a), with parts of the landslide coming to a halt during the fall of 2012 and 2013 (Figure 3). We find that a simple model of time-dependent pore pressure diffusion can explain the nonlinear relationship between precipitation and seasonal deformation captured by IC1 and IC2 in the ICA of the TSX time series.

5 Conclusions

A series of signal processing methods (ICA, PCA, and FCF) performed on InSAR time series from 2009 to 2014 of the EBH provides unique insight into the mechanisms driving observed ground surface displacements in the area of the BLS. Through FCF analysis we identify and correct for mean seasonal deformation observed away from the BLS, revealing an underlying trend of annually accelerated landslide displacements. Through PCA and ICA we separate four independent spatiotemporal components of the deformation, illustrating different geomechanical processes on and around the landslide. The first two components capture the sensitivity of landslide deformation rates to annual and long-term climate conditions. We observe a slowdown of landslide movement associated with the onset of severe drought conditions in 2012, and seasonal precipitation-modulated landslide deformation with an ~44 day lag. The correlation of landslide motion and precipitation at variable time scales is well explained by a simple model of time-dependent pore pressure diffusion. On and off the landslide we characterize two additional components of broadly distributed and spatially heterogeneous seasonal deformation, associated with the shrink/swell cycle of near-surface soils and a combination of annual groundwater heave processes and thermal expansion of structures. The ability to differentiate and quantify these processes to the extent illustrated is a significant advancement toward predicting the magnitude and spatiotemporal distribution of seasonal ground deformation in slow-moving landslides.

Acknowledgments

We gratefully acknowledge our financial support from the Lawrence Berkeley National Laboratory, Earth Science Division Director's Fund; the National Aeronautics and Space Administration (NASA) through grant NNX12AQ32G; and the Civil and Environmental Engineering Department and Cahill Chair at the University of California Berkeley. TerraSAR-X data were provided through a user license by the German Space Agency (DLR). The processed data used in our analysis are included with and described in the accompanying supplement. We thank two anonymous reviewers, Al Handwerger, Mong-Han Huang, and the Associate Editor for their constructive comments, which helped improve the quality of this paper.

References

Beaty, C. B. (1956). Landslides and slope exposure. *The Journal of Geology*, 64(1), 70– 74. https://doi.org/10.1086/626317

Bennett, G. L., Roering, J. J., Mackey, B. H., Handwerger, A. L., Schmidt, D. A., & Guillod, B. P. (2016). Historic drought puts the brakes on earthflows in Northern California. *Geophysical Research Letters*, 43, 5725– 5731. https://doi.org/10.1002/2016gl068378

Bishop, C. C., Knox, R. D., Chapman, R. H., Rodgers, D. A., & Chase, G. B. (1973). Geological and geophysical investigations for Tri-Cities (El Cerrito, Richmond, and San Pablo) seismic safety and environmental resources

study. California Division of Mines and Geology (Preliminary Report 19, 44 p.).

Bürgmann, R., Rosen, P. A., & Fielding, E. J. (2000). Synthetic aperture radar interferometry to measure Earth's surface topography and its deformation. *Annual Review of Earth and Planetary Sciences*, 28(1), 169– 209. https://doi.org/10.1146/annurev.earth.28.1.169

Cattell, R. B. (1966). The scree test for the number of factors. *Multivariate Behavioral Research*, 1(2), 245– 276. https://doi.org/10.1207/s15327906mbr0102_10

Cattell, R. B., & Jaspers, J. (1967). A general plasmode (no. 30-10-5-2) for factor analytic exercises and research. *Multivariate Behavioral Research Monographs*, 67-3, 211.

Chaussard, E., Bürgmann, R., Shirzaei, M., Fielding, E. J., & Baker, B. (2014). Predictability of hydraulic head changes and characterization of aquifer-system and fault properties from InSAR-derived ground deformation. *Journal of Geophysical Research: Solid Earth*, 119, 6572– 6590. https://doi.org/10.1002/2014JB011266

Chaussard, E., Bürgmann, R., Fattahi, H., Johnson, C. W., Nadeau, R., Taira, T., & Johanson, I. (2015). Interseismic coupling and refined earthquake potential on the Hayward-Calaveras fault zone. *Journal of Geophysical Research: Solid Earth*, 120, 8570– 8590. https://doi.org/10.1002/2015JB012230

Colesanti, C., & Wasowski, J. (2006). Investigating landslides with space-borne Synthetic Aperture Radar (SAR) interferometry. *Engineering Geology*, 88(3-4), 173– 199. https://doi.org/10.1016/j.enggeo.2006.09.013

Cruden, D. M., & Varnes, D. J. (1996). Landslides: Investigation and mitigation. Chapter 3—Landslide types and processes Transportation research board special report (Vol. 247).

Delbridge, B. G., Bürgmann, R., Fielding, E., Hensley, S., & Schulz, W. H. (2016). Three-dimensional surface deformation derived from airborne interferometric UAVSAR: Application to the Slumgullion landslide. *Journal of Geophysical Research: Solid Earth*, 121, 3951– 3977. https://doi.org/10.1002/2015JB012559

Dibblee, T. W. Jr. (1980). Preliminary geologic map of the Briones Valley Quadrangle, Alameda and Contra Costa counties, California. United States Geological Survey (Open-File Report 80–539). Retrieved from http://pubs.er.usgs.gov/publication/ofr80539

Dussauge, C., Grasso, J.-R., & Helmstetter, A. (2003). Statistical analysis of rockfall volume distributions: Implications for rockfall dynamics. *Journal of Geophysical Research*, 108(B6), 11. https://doi.org/10.1029/2001JB000650

Eineder, M., Adam, N., Bamler, R., Yague-Martinez, N., & Breit, H. (2009). Spaceborne spotlight SAR interferometry with TerraSAR-X. *IEEE Transactions on Geoscience and Remote Sensing*, 47(5), 1524– 1535. https://doi.org/10.1109/tgrs.2008.2004714

Ferretti, A., Prati, C., & Rocca, F. (2001). Permanent scatterers in SAR interferometry. *IEEE Transactions on Geoscience and Remote Sensing*, 39(1), 8– 20. https://doi.org/10.1109/36.898661

Ferretti, A., Fumagalli, A., Novali, F., Prati, C., Rocca, F., & Rucci, A. (2011). A new algorithm for processing interferometric data-stacks: SqueeSAR. *IEEE Transactions on Geoscience and Remote Sensing*, 49(9), 3460– 3470. https://doi.org/10.1109/tgrs.2011.2124465

Field, E. H., & 2014-WGCEP (2015). UCERF3: A new earthquake forecast for California's complex fault system. *Fact Sheet*, 1– 6. https://doi.org/10.3133/fs20153009

Fuyii, Y. (1969). Frequency distribution of landslides caused by heavy rain-fall. *Journal of the Seismological Society of Japan*, 22(3), 244– 247. https://doi.org/10.4294/zisin1948.22.3_244

Gilliam, H. (2002). *Weather of the San Francisco Bay Region* (Vol. 63). Berkeley, CA: University of California press.

Graymer, R. W. (Cartographer) (2000). Geologic map and map database of the Oakland metropolitan area, Alameda, Contra Costa, and San Francisco Counties, California.

Graymer, R. W., Jones, D. L., & Brabb, E. E. (1994). Preliminary geologic map emphasizing bedrock formations in Contra Costa County, California; a digital database. Report (Open-File Report 94–622). Retrieved from http://pubs.er.usgs.gov/publication/ofr94622

Gualandi, A., Avouac, J.-P., Galetzka, J., Genrich, J. F., Blewitt, G., Adhikari, L. B., et al. (2017). Pre- and post-seismic deformation related to the 2015, Mw7.8 Gorkha earthquake, Nepal. *Tectonophysics*, 714–715, 90– 106. https://doi.org/10.1016/j.tecto.2016.06.014

Handwerger, A. L., Roering, J. J., & Schmidt, D. A. (2013). Controls on the seasonal deformation of slow-moving landslides. *Earth and Planetary Science Letters*, 377-378, 239– 247. https://doi.org/10.1016/j.epsl.2013.06.047

Handwerger, A. L., Rempel, A. W., Skarbek, R. M., Roering, J. J., & Hilley, G. E. (2016). Rate-weakening friction characterizes both slow sliding and catastrophic failure of landslides. *Proceedings of the National Academy of Sciences of the United States of America*, 113(37), 10,281– 10,286. https://doi.org/10.1073/pnas.1607009113

Hilley, G. E., Bürgmann, R., Ferretti, A., Novali, F., & Rocca, F. (2004). Dynamics of slow-moving landslides from permanent scatterer analysis. *Science*, 304(5679), 1952– 1955. https://doi.org/10.1126/science.1098821

Hooper, A., Bekaert, D., Spaans, K., & Arıkan, M. (2012). Recent advances in SAR interferometry time series analysis for measuring crustal deformation. *Tectonophysics*, 514, 1– 13. https://doi.org/10.1016/j.tecto.2011.10.013

Iverson, R. M., & Major, J. J. (1987). Rainfall, ground-water flow, and seasonal movement at Minor Creek landslide, northwestern California: Physical interpretation of empirical relations. *Geological Society of America Bulletin*, 99(4), 579– 594. https://doi.org/10.1130/0016-7606(1987)99%3C579:rgfasm%3E2.0.co;2

Jackson, D. A. (1993). Stopping rules in principal components analysis: A comparison of heuristical and statistical approaches. *Ecology*, 74(8), 2204–2214. https://doi.org/10.2307/1939574

Ji, K. H., & Herring, T. A. (2011). Transient signal detection using GPS measurements: Transient inflation at Akutan volcano, Alaska, during early 2008. *Geophysical Research Letters*, 38, L06307. https://doi.org/10.1029/2011GL046904

Keefer, D. K., & Johnson, A. M. (1983). Earth flows: morphology, mobilization, and movement. United States Geological Survey (professional paper 1264, 56 p.). Retrieved from http://pubs.er.usgs.gov/publication/pp1264

Kropp, A. (Cartographer) (1995). Landslides of the Berkeley Hills. Retrieved from http://akropp.com/wp-content/uploads/2013/07/berkeley_hills_slide_map.pdf

Kropp, A. (2010). Berkeley Hills landslide-induced property line movement under both static and earthquake conditions. In K Knudson (Ed.), *Proceedings of the Third Conference on Earthquake Hazards (2008), Eastern San Francisco Bay Area*. California Geological Survey Special Report 219.

Kropp, A., & Lettis, W. (2002). *Blakemont Area Geologic Study, El Cerrito and Kensington California*. Berkeley CA: Engineering Consulting Report. Alan Kropp and Associates.

Lacroix, P., Perfettini, H., Taipe, E., & Guillier, B. (2014). Coseismic and postseismic motion of a landslide: Observations, modeling, and analogy with tectonic faults. *Geophysical Research Letters*, 41, 6676– 6680. https://doi.org/10.1002/2014GL061170

Larsen, I., Montgomery, D., & Korup, O. (2010). Landslide erosion controlled by hillslope material. *Nature Geoscience; London*, 3(4), 247– 251. https://doi.org/10.1038/ngeo776

Lei, L., & Bürgmann, R. (2010). Application of PSI to investigate the Berkeley Hills landslides. AGU Fall Meeting. Retrieved from http://adsabs.harvard.edu/abs/2010AGUFM.G13A0666L

Lischeid, G. (2009). Non-linear visualization and analysis of large water quality data sets: A model-free basis for efficient monitoring and risk

assessment. *Stochastic Environmental Research and Risk Assessment*, 23(7), 977– 990. https://doi.org/10.1007/s00477-008-0266-y

Manly, B. F. J. (1986). Randomization and regression methods for testing for associations with geographical, environmental and biological distances between populations. *Researches on Population Ecology*, 28(2), 201– 218. https://doi.org/10.1007/bf02515450

Ng, C. W. W., Zhan, L. T., Bao, C. G., Fredlund, D. G., & Gong, B. W. (2003). Performance of an unsaturated expansive soil slope subjected to artificial rainfall infiltration. *Geotechnique*, 53(2), 143– 157. https://doi.org/10.1680/geot.2003.53.2.143

Nilsen, T. H., & Turner, B. L. (1975). Influence of rainfall and ancient landslide deposits on recent landslides (1950–71) in urban areas of Contra Costa County, California. United States Geological Survey (Bulletin 1388) (18 p.). Retrieved from http://pubs.er.usgs.gov/publication/b1388

Quigley, K. C., Bürgmann, R., Giannico, C., & Novali, F. (2010). Seasonal acceleration and structure of slow moving landslides in the Berkeley Hills. K Knudsen (Ed.), *Proceedings of the Third Conference on Earthquake Hazards (2008), Eastern San Francisco Bay Area*. California Geological Survey Special Report 219. Retrieved from http://www.academia.edu/364912/Slow_Moving_Landslides_of_the_Berkeley_Hills

Richman, M. B. (1986). Rotation of principal components. *Journal of Climatology*, 6(3), 293– 335. https://doi.org/10.1002/joc.3370060305

Rosenbalm, D. C. (2013). Volume change behavior of expansive soils due to wetting and drying cycles. (doctor of philosophy), Arizona State University.

Savage, J. C. (1988). Principal component analysis of geodetically measured deformation in Long Valley Caldera, Eastern California, 1983–1987. *Journal of Geophysical Research*, 93(B11), 13,297– 13,305. https://doi.org/10.1029/JB093ib11p13297

Seager, R., Hoerling, M., Schubert, S., Wang, H., Lyon, B., Kumar, A., et al. (2015). Causes of the 2011–14 California drought. *Journal of Climate*, 28(18), 6997– 7024. https://doi.org/10.1175/jcli-d-14-00860.1

Seidelman, P., & Deane, R. T. (1994). Geotechnical investigation of the Blakemont landslide located in Kensington and El Cerrito, California. Engineering Consulting Report. Walnut Creek, CA: Seidelman Associates, Inc.

Shirzaei, M., & Bürgmann, R. (2013). Time-dependent model of creep on the Hayward fault from joint inversion of 18 years of InSAR and surface creep data. *Journal of Geophysical Research: Solid Earth*, 118, 1733– 1746. https://doi.org/10.1002/jgrb.50149

Simonett, D. S. (1967). Landslide distribution and earthquakes in the Bewani and Torricelli Mountains, New Guinea. In J. N Jennings & J. A Mabbutt (Eds.),

Landform Studies From Australia and New Guinea (pp. 64– 84). New York: Cambridge University Press.

Simoni, A., Ponza, A., Picotti, V., Berti, M., & Dinelli, E. (2013). Earthflow sediment production and Holocene sediment record in a large Apennine catchment. *Geomorphology*, 188, 42– 53. https://doi.org/10.1016/j.geomorph.2012.12.006

Tabachnick, B. G., Fidell, L. S., & Osterlind, S. J. (2001). *Using Multivariate Statistics* (3rd ed.). New York: Harper Collins.

Terzaghi, K. (1950). Mechanism of landslides. In S. Paige (Ed.), *Application of Geology to Engineering Practice: Berkey Volume* (pp. 83– 123). New York: The Geological Society of America. https://doi.org/10.1130/berkey.1950.83

Tofani, V., Raspini, F., Catani, F., & Casagli, N. (2013). Persistent Scatterer Interferometry (PSI) technique for landslide characterization and monitoring. *Remote Sensing*, 5(12), 1045– 1065. https://doi.org/10.3390/rs5031045

Wackernagel, H. (1988). Geostatistical techniques for interpreting multivariate spatial information. In C. F Chung, A. G Fabbri, & R Sinding-Larsen (Eds.), *Quantitative Analysis of Mineral and Energy Resources* (pp. 393– 409). Dordrecht, Netherlands: Springer. https://doi.org/10.1007/978-94-009-4029-1_24

Wasowski, J., & Bovenga, F. (2014). Investigating landslides and unstable slopes with satellite multi temporal interferometry: Current issues and future perspectives. *Engineering Geology*, 174, 103– 138. https://doi.org/10.1016/j.enggeo.2014.03.003